metals

Article

Effects of Sintering Pressure and Co Content on the Microstructure and Mechanical Performance of WC–Co Cemented Carbides

Jinhu Ju [1], Dan Huang [2], Haitao Xu [1,*], Duo Dong [1], Jiangpeng Lou [3], Yuan Xu [1], Jiao Shi [1] and Liu Zhu [1,*]

[1] School of Materials Science and Engineering, Taizhou University, Taizhou 318000, China; 15968662912@163.com (J.J.)
[2] Taizhou Institute of Product Quality and Safety Inspection, Taizhou 318000, China
[3] Hengdian Group DMEGC Magnetics Co., Ltd., Jinhua 322100, China
* Correspondence: haitaoxu@tzc.edu.cn (H.X.); zhuliu@tzc.edu.cn (L.Z.)

Abstract

The fabrication of WC-based cemented carbides faced challenges including inhomogeneous composition and grain coarsening. To solve these problems, WC–Co cemented carbides were fabricated via spark plasma sintering (SPS) using core–shell WC–Co powders prepared by an electroless plating method. The effects of sintering pressure and Co content on the microstructure and mechanical properties of the cemented carbides were investigated. The results showed that, with increasing sintering pressure, the relative density of the sintered samples was improved (98.4–99.6%) while the grains were coarsened (0.94–1.07 μm). The optimal properties (fracture toughness 11.11 MPa·m$^{1/2}$, and hardness 2100.3 HV30) were obtained when sintered with a pressure of 20 MPa. Grain coarsening at higher pressure (30 MPa) reduced the toughness of the cemented carbides. When the Co content was increased from 3 wt.% to 8 wt.%, fracture toughness was improved while the hardness of the cemented carbides was reduced, attributed to the intrinsic high toughness and low hardness of the Co phase. The WC–8 wt.% Co cemented carbides exhibited optimized synergic mechanical performance (hardness of 1874.2 HV30 and fracture toughness of 13.77 MPa·m$^{1/2}$). This work elucidated the relationship between the key sintering parameters (pressure and Co content) and the microstructure and mechanical properties of the cemented carbides. The achievements obtained provide a theoretical foundation for high-quality fabrication of the WC–Co cemented carbides.

Keywords: WC–Co cemented carbide; SPS; sintering pressure; Co content; microstructure

check for updates

Academic Editor: Ivanovich Estrada-Guel

Received: 14 July 2025
Revised: 17 August 2025
Accepted: 20 August 2025
Published: 22 August 2025

Citation: Ju, J.; Huang, D.; Xu, H.; Dong, D.; Lou, J.; Xu, Y.; Shi, J.; Zhu, L. Effects of Sintering Pressure and Co Content on the Microstructure and Mechanical Performance of WC–Co Cemented Carbides. *Metals* **2025**, *15*, 930. https://doi.org/10.3390/met15090930

Copyright: © 2025 by the authors. Licensee MDPI, Basel, Switzerland. This article is an open access article distributed under the terms and conditions of the Creative Commons Attribution (CC BY) license (https://creativecommons.org/licenses/by/4.0/).

1. Introduction

WC-based cemented carbides find extensive application in the manufacture of cutting tools, mining drills, molds, and other machining components, attributed to their exceptional hardness, superior wear resistance, and notable impact toughness [1,2]. The operational durability and productivity of such manufacturing equipment are fundamentally governed by the performance characteristics of WC-based cemented carbides. Consequently, the high-quality fabrication of cemented carbides has always been the research hotspot in this field [3,4]. With components in high-end manufacturing subjected to increasingly harsh service conditions, conventional cemented carbides face challenges such as short lifespans and suboptimal properties. These challenges necessitate the advancement of cemented carbides exhibiting enhanced mechanical characteristics.

WC–Co composite powders serve as foundational starting materials for cemented carbide production, exerting a decisive influence on the characteristics of the resulting sintered products. For the fabrication of the WC–Co composite powders, methods including mechanical mixing, high-energy ball milling, self-propagating high-temperature synthesis, and electroless plating are used. The mechanical mixing method offers simple processing and low cost, but often leads to inhomogeneous composition of the mixed powders. High-energy ball milling enables the lowering of reaction activation energy while mitigating compositional segregation in constituent powders [5]. However, impurities may be introduced and the prolonged milling may cause the smashing of the WC particles, which adversely affects the properties of the carbides. The self-propagating high-temperature synthesis method features rapid reaction kinetics and high energy efficiency. The high-temperature process volatilizes impurities, thereby enhancing product purity [6]. Nevertheless, the reaction process is difficult to control, and the WC may decompose into W_2C or W at such extremely high temperatures. The electroless plating method is based on autocatalytic redox reactions. Core–shell WC–Co composite powders can be fabricated via deposition of metallic species onto WC substrate surfaces. This method is particularly suitable for preparing coated WC–binder composite powders. The core–shell structure formed enables the uniform encapsulation of WC particles by the Co binder phase through establishing chemical bonding between the WC and binder [7]. Research confirms that uniform binder layers on WC powders are attainable through electroless plating, employing $NaH_2PO_2 \cdot H_2O$ as a reductant and $Na_3C_6H_5O_7 \cdot 2H_2O$ as a complexant [8]. This approach consequently enhances both the microstructural characteristics and mechanical performance of WC-based cemented carbides.

Recent years have witnessed the increasing diversification in cemented carbide sintering techniques. Traditional methods like vacuum sintering and hot-press sintering have drawbacks such as excessive energy consumption, prolonged processing times, and grain coarsening. In contrast, powder densification can be achieved within minutes through the SPS method under the synergistic effects of a pulsed current and axial pressure. This technique was characterized by its swift densification, low operating temperatures, and high efficiency, thereby effectively reducing WC coarsening throughout the sintering cycle. The influence of sintering temperature on microstructure development and mechanical response in SPS-processed WC–Co cemented carbides has been systematically examined in comprehensive research. It is generally observed that within the temperature range of 1200–1500 °C, lower sintering temperatures predominantly promote solid-state sintering, during which the dissolution and precipitation of WC are relatively mild, and insufficient liquid-phase Co filling leads to a higher porosity in the alloy. Elevated sintering temperatures promote systematic enhancement in both densification behavior and WC grain dimensions within cemented carbide structures. Nevertheless, excessively high sintering temperatures promote the growth of abnormal grains, thereby inducing a marked deterioration in the hardness and fracture toughness of these materials [9,10]. Notably, sintering pressure constitutes a critical SPS parameter that concurrently governs WC grain size distribution, Co binder migration kinetics, porosity evolution, and resultant mechanical characteristics in cemented carbides. Nevertheless, the fundamental consolidation mechanisms operating under varying pressure regimes remain inadequately elucidated. The binder-phase Co demonstrates remarkable energy absorption capability when cracks propagate into Co-rich regions due to its excellent toughness and plasticity. This effectively impedes crack propagation into the alloy interior, thereby enhancing overall mechanical performance.

To elucidate the synergistic mechanism between sintering pressure and Co content for WC–Co composite powders, the core–shelled WC–Co composite powder prepared via electroless plating was employed to fabricate cemented carbides through SPS. The

effects of sintering pressure and Co content on the microstructural evolution and resultant mechanical properties (hardness, fracture toughness) were systematically investigated. The intrinsic relationship between the critical SPS parameters and the forming quality of WC–Co cemented carbides derived from the core–shell precursor was elucidated. Through this targeted investigation, the optimal combination of sintering pressure and the corresponding Co content was established, providing crucial technical and theoretical support for the efficient and high-quality fabrication of WC–Co cemented carbides.

2. Materials and Methods

2.1. Preparation of WC–Co Composite Powders

The present investigation employed WC powder (99.9% purity, mean particle size: 0.90 μm) sourced from Xiamen Golden Egret Special Alloy Co., Ltd. (Xiamen, China). The WC powder was first subjected to ultrasonic cleaning in ethanol to remove surface oils and impurities. Subsequently, the powder was rinsed with deionized water and settled for over 12 h, with subsequent convection drying at 60 °C for 5 h. Next, the WC powder was added to an activation solution with a loading amount of 200 g/L, as illustrated in Figure 1a. Table 1 details the formulation of the activation solution employed. All chemical reagents used were manufactured by Aladdin Company (Shanghai, China) with a HNO_3:HF concentration ratio is 5:4. Ultrasonic assistance (frequency: 50 kHz, power: 300 W) was applied during the activation process for 30 min. Following activation treatment, the powder underwent thorough deionized water washing and subsequent drying, yielding surface-activated WC powders.

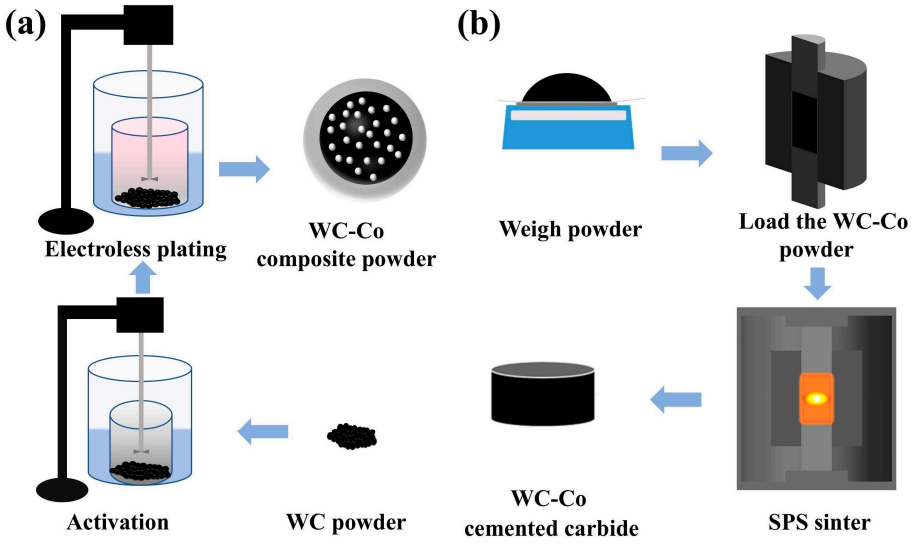

Figure 1. Schematic images showing the preparation process of the WC–Co cemented carbides: (**a**) fabrication of WC–Co composite powder; (**b**) sintering of WC–Co cemented carbides.

Table 1. Activation solution formulation components.

Reagent	Concentration
65% HNO_3	20~60 mL/L
40% HF	30~50 mL/L
NH_4F	2~4 g/L

Activated WC particulates were immersed in autocatalytic deposition baths at solid loadings of 150, 90, and 50 g/L, yielding WC–3Co, WC–5Co, and WC–8Co composite powders, respectively. The composition of the electroless plating solution is detailed

in Table 2. During the planting process, the solution was maintained at 75–85 °C until gas bubbles emerged, which indicated the reactions began. Subsequently, the mixture was transferred into an ultrasonic bath for ultrasonically assisted electroless Co plating, accompanied by mechanical stirring with a rate of 100 r/min. The electroless Co plating process was considered complete when no further gas bubbles were generated in the solution. The metallized particulates were subsequently subjected to DI water rinsing and convection drying (60 °C, 8 h), fabricating WC–Co composites with nominal cobalt contents of 3, 5, and 8 wt.%, respectively.

Table 2. Compositions of the electroless plating solution.

Reagent	Concentration
$CoSO_4 \cdot 7H_2O$	20~30 g/L
$NaH_2PO_2 \cdot H_2O$	20~30 g/L
$Na_3C_5H_5O_7 \cdot 2H_2O$	40~50 g/L
H_3BO_3	20~30 g/L
NaOH	For adjusting the pH within 10~11

2.2. Spark Plasma Sintering

WC–Co powders were consolidated using a Fuji SPS-212H spark plasma sintering system (Fuji Electronic Industrial Co., Ltd., Tsurugashima, Japan), as shown in Figure 1b. First, 5 g of WC–Co composite powder was weighed and loaded into a graphite mold, with the graphite paper applied to protect the mold. The graphite mold was then wrapped with graphite wool for thermal insulation during heating. The mold was subsequently mounted in the SPS furnace chamber, where electric heating and pressure was applied. Before sintering, the furnace was vacuumized and maintained at 10^{-1} Pa. According to studies before [11,12], the sintering experiments were conducted at 1430 °C to ensure the melting of Co. With the rapid heating rate during SPS, the relative short soaking duration of 5 min was set. The sintering pressure, 10, 20 and 30 MPa, was selected to study the evolution trend of the microstructure and mechanical properties of the alloys.

2.3. Microstructural Characterization

The sintered cemented carbide specimens underwent sequential surface finishing with 100, 400, 800, and 1000 mesh diamond discs, followed by polishing with diamond suspensions for the metallographic samples. Microstructural characterization was performed using a scanning electron microscope (SEM, Hitachi S-4800, Tokyo, Japan) to examine the morphology, size, and size distribution of WC powders, activated powders, WC–Co composite powders, and sintered specimens. The SEM characterization was conducted with an accelerating voltage of 15 kV and a beam current of 9 μA. A field-emission transmission electron microscope (TEM, Tecnai G2 F30, FEI Company, Hillsboro, OR, USA) was employed to investigate the micromorphology of the activated WC powder. Phase analysis of the WC–Co composite powders was performed via the X-ray diffractometer (XRD, Bruker D8 Advance, Karlsruhe, Germany). Measurements were conducted using Cu Kα radiation (λ = 1.5406 Å) with an accelerating voltage of 40 kV and a tube current of 40 mA. The 2θ scanning angle ranges from 20° to 90° and was detected with a rate of 8 °/min. The obtained XRD patterns were analyzed using MDI Jade 9.0 software. Phase identification was achieved by comparing the diffraction patterns with the standard PDF database.

2.4. Mechanical Characterization

The Vickers hardness test was conducted using an HVS-50ZL digital Vickers hardness tester manufactured by Huaying (Laizhou, China), with a test load of 30 kgf and a dwell

time of 10 s. The average hardness of the alloys was obtained after 5 indents for each sample. After testing, the indentations shown in Figure 2 were obtained (L: crack length, and D: indentation diagonal length). The K_{IC} was then evaluated in accordance with the Palmqvist toughness Formula (1) [13].

$$K_{IC} = 0.15 \times \sqrt{\frac{H}{\sum L}} \quad (1)$$

In Formula (1): fracture toughness, denoted by K_{IC}, is expressed in MPa·m$^{1/2}$. The Vickers hardness (H) of the sample (unit: N/mm^2 or equivalently to MPa). The parameter $\sum L$ represents the total length (in mm) of radial cracks propagating from the indentation corners.

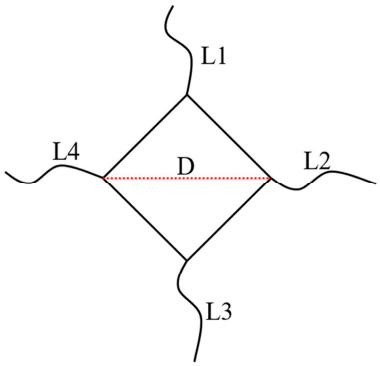

Figure 2. Schematic of the indentation morphology.

3. Results and Discussion

3.1. Microstructural Analysis of Coated WC–Co Composite Powders

Figure 3 shows the SEM morphology of the powders under different processing conditions. In Figure 3a, the raw WC powders show the smooth surface. After non-precious metal activation, some groove and stage defects were formed on the WC surface (as indicated by the red square in Figure 3b), improving the roughness of the WC surface. The activation pretreatment increases the activated area and the surface energy of WC powders, which provides proper reaction conditions for the subsequent plating of Co. In Figure 3c, it is found that uniform flocculent Co coating is present on the WC surface, forming the core–shelled WC–Co composite powders. EDS analysis was also performed for these powders and the results are shown in Figure 3. It can be seen that no impurities were introduced after the activation treatment. Figure 3c shows that the C, W and the Co elements were evenly distributed.

Figure 4 presents the TEM images of the activated WC powders. It can be seen that lattice defects, including stacking faults and dislocations, are present on the activated WC powder surface [14]. The results obtained agree with the previous study [15], which showed dislocations formed on the WC surface after activation. These defects expose unsaturated atoms and thus create an ideal environment for redox reactions of the WC particles. Meanwhile, the surrounding high-energy regions provide nucleation sites for metal particle growth during the subsequent electroless plating process. As shown in Figure 4b, the diffraction spots correspond to the WC [0001] crystal plane, and the stacking fault extends along the [$2\bar{1}\bar{1}0$] crystal direction.

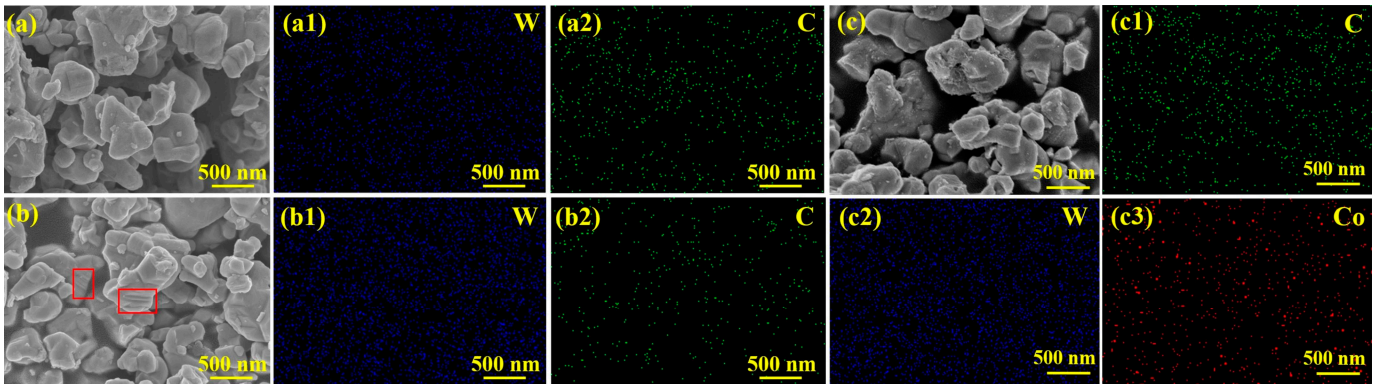

Figure 3. SEM and EDS images of the powders: (**a**,**a1**,**a2**) raw WC powder; (**b**,**b1**,**b2**) activated WC powder; (**c**,**c1**–**c3**) electroless-plated WC–Co composite powder.

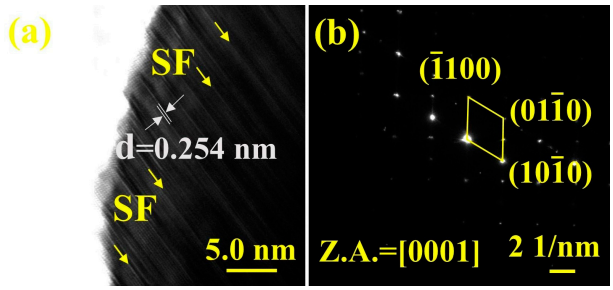

Figure 4. TEM images of the activated WC powder: (**a**) bright field image; and (**b**) SAED pattern.

The essence of electroless plating of Co lies in the selective reduction reaction and the deposition of Co^{2+} on WC powder surfaces. The chemical reaction involved is: $Co^{2+} + 2H_2PO_2^- + 2H_2O \rightarrow Co + 2H_2PO_3^- + 2H^+ + H_2\uparrow$. During this reaction, Co^{2+} is reduced by the $H_2PO_2^-$ into Co metal, which is then deposited on the WC surface. This process consists of two stages: dehydrogenation and reduction reactions. During the dehydrogenation stage, $NaH_2PO_2 \cdot H_2O$ released electrons through dehydrogenation reactions at active sites of the WC particles. In the reduction stage, the Co^{2+} was reduced to metallic Co by the electrons with the hydrogen evolution reactions occurring simultaneously [16]. Owing to the high catalytic activity of the activated WC powder surface, the efficiency of dehydrogenation reactions was significantly enhanced [17]. Meanwhile, defect sites lowered the energy barrier for Co nucleation, promoting its growth on WC particles. Figure 3c reveals a uniform flocculent Co coating on the composite powder surface. XRD analysis (Figure 5) confirms that the powder consists solely of WC and metallic Co phases, with no detectable Co^{2+}, indicating complete reduction to elemental Co.

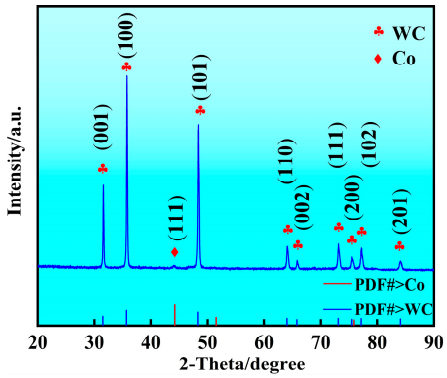

Figure 5. XRD patterns of the WC–Co composite powder obtained through the electroless plating method.

3.2. Effects of Sintering Pressure on the Microstructure of Cemented Carbides

The microstructure and the grain size of WC–5 wt.% Co cemented carbides prepared by SPS under different sintering pressures are shown in Figure 6. Table 3 presents the elemental composition of the three samples, and the detection areas A, B, C were shown in Figure 6a1,b1,c1. It can be seen that the Co content in all three samples is approximately 5 wt.%, consistent with the nominal Co content calculated based on the loading amount. The results show that the average grain sizes of the samples sintered at 10 and 20 MPa were 0.97 and 0.94 μm, respectively, with no significant variation. At 30 MPa sintering pressure, cemented carbides exhibit significant grain coarsening, with the average grain size reaching 1.12 μm and the maximum grain size approaching 2.5 μm (Figure 5). These microstructural changes confirm that excessive pressure induces abnormal grain growth.

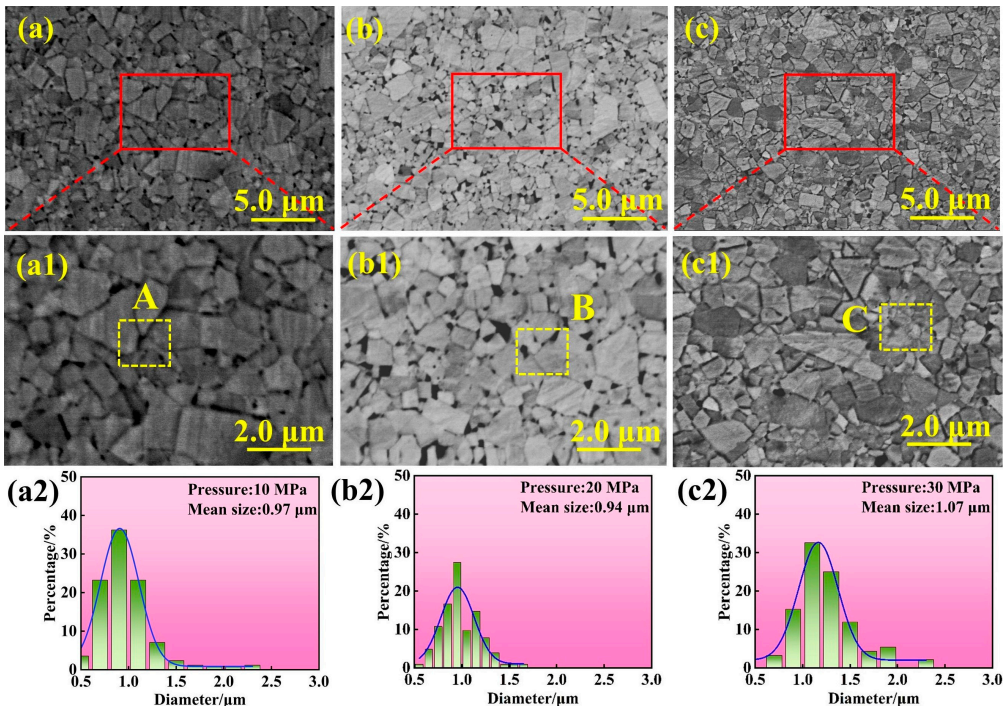

Figure 6. Microstructure and grain distribution of WC–5Co cemented carbide sintered under different pressures: (**a**,**a1**,**a2**) 10 MPa; (**b**,**b1**,**b2**) 20 MPa; (**c**,**c1**,**c2**) 30 MPa.

Table 3. EDS compositional analysis results for the phases in Figure 6.

Area	Compositions (wt.%)		
	W	C	Co
A	84.56	10.13	5.31
B	84.62	9.35	6.03
C	84.28	10.88	4.84

During the sintering process, the growth should be explained as a coalescence phenomenon. During the initial sintering stage, the gaps between WC particles were reduced, facilitating grain-to-grain contact. This created favorable conditions for particle coalescence, resulting in the high contiguity of WC particles and significantly promoting grain growth. This mechanism is considered the primary cause of WC particle coarsening. Moreover, the WC dissolves in the liquid Co [18]. The oversaturated W and C reprecipitates onto the undissolved WC particles, resulting in the continuous grain growth of the WC grains. During the cooling process, the growth of the WC particles further promotes the reduced

dissolution of WC in the liquid. This process is known as Oswald maturation [19], which is one of the reasons for the coarsening of the WC particles. When sintered at higher pressure (30 MPa), the high contiguity of WC under such high sintering pressure leads to grain growth, mainly through coalescence. Furthermore, the enhanced flowability of the liquid facilitated the diffusion of WC in the Co phase. Therefore, the reprecipitation of WC on the surfaces of larger WC grains was also promoted. Consequently, abnormal grain growth of the cemented carbides occurs.

Figure 7 illustrates the relationship between displacement of the punch and sintering time. Sintering occurs through four sequential stages: Stage I—initial sintering, stage II—thermal expansion of the compact, stage III—liquid phase formation and stage IV—the cooling stage. In the initial sintering stage, powders were rearranged under axial pressure, leading to increased shrinkage displacement. As the temperature rose, the thermal expansion (stage II) of the compact powders partially offset the punch displacement, resulting in the plateau observed in Figure 7. During stage II, solid-state sintering densification occurred between powders through surface diffusion, and slowed shrinkage displacement. In stage III, the samples shrank rapidly as the liquid phase formed at high temperatures. In such a case, the displacement of the punch reached the maximum value. In stage IV, during the cooling of the sample, radial shrinkage of the mold occurred due to the different thermal expansion coefficients between the graphite mold and WC, resulting in a slight decrease in alloy compression displacement.

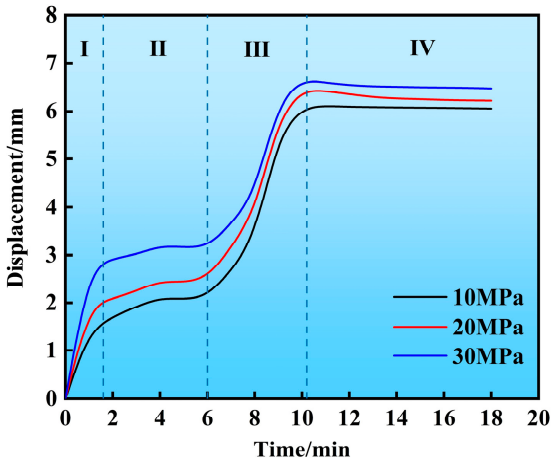

Figure 7. Time–displacement curves of the WC–Co cemented carbide sintered under different pressures.

It is also shown in Figure 7 that the displacement of the sintering punch is gradually enhanced with increasing sintering pressure, thereby enhancing densification in WC cemented carbides (Figure 8). During SPS processing, discharge effects arise within interparticle gaps through the simultaneous application of a pulsed current and pressure to WC–Co composite powders. Under these conditions, local high temperatures occurred with the plasma, created by the ionized gas in the particle gaps. As a result, particle surfaces evaporated and melted, forming liquid Co and developing necks at particle contact points [20]. The rapid cooling of these necks resulted in a vapor pressure lower than that inside the powder particles. Therefore, increasing the sintering pressure could enhance the evaporation–solidification phenomenon, thereby accelerating the densification of WC–Co alloys.

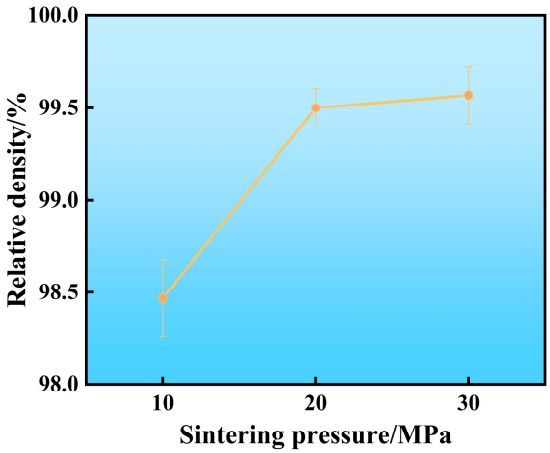

Figure 8. The relative density of WC–Co cemented carbides sintered under different pressures.

An increased sintering pressure improves liquid Co mobility on particle surfaces. Meanwhile, under the combined effects of rapid heating and discharge phenomena, the grain surface remains in a highly activated state. This intensified bulk diffusion and grain boundary diffusion between the particles, improving the flow of WC grains [21]. These mechanisms accelerated pore closure during sintering, thereby reducing porosity and enhancing densification in WC–Co cemented carbides. When the sintering pressure was increased from 10 MPa to 20 MPa, the relative density showed significant improvement, reaching 99.6%. This maintains the same level compared with the cemented carbides prepared by the conventional sintering method [22]. When the sintering pressure is increased to 30 MPa, the relative density shows no significant improvement compared to that at 20 MPa.

3.3. Effects of Sintering Pressure on the Mechanical Properties of the Cemented Carbides

Vickers hardness evolution under varying sintering pressures (Figure 9) reveals a positive correlation: Higher pressures yield increased hardness in WC–Co cemented carbides. Following the hardness modeling framework for cemented carbides ($H = Kd^{-a}e^{-bp}$), reduced porosity (p) directly contributes to enhanced hardness (H) [23]. When sintered at 10 MPa, the alloy exhibits minimum hardness due to incomplete densification, as shown in Figure 8. Under 2a 0 MPa sintering pressure, the interparticle contact area was expanded, which helped to eliminate the pores and improve the density of the alloys. For this, the hardness of the cemented carbide was increased according to the hardness model. Furthermore, no grain coarsening occurs at 20 MPa, as shown in Figure 6. Therefore, hardness improvement stemmed from grain refinement. While sintered at 30 MPa pressure near-complete densification (99.7%) was achieved. However, the detrimental WC grain growth posed negative effects to the mechanical properties of the alloy. Consequently, hardness enhancement was insignificant beyond 20 MPa.

Figure 10 displays fracture toughness evolution in WC–Co cemented carbides versus sintering pressure, revealing an initial increase followed by a decrease. When sintered at 10 MPa, the pores generated significantly weaken the toughness of WC–Co alloys. When the pressure increases to 20 MPa, the reduced porosity effectively increases the load-bearing area within the alloys. This can also avoid stress concentration at pore edges [24], thus enhancing fracture toughness through improved crack propagation resistance. At this sintering pressure, both fracture toughness and hardness show improvements with varying degrees compared with that obtained via high-pressure sintering [25]. When the pressure exceeds 30 MPa, the sample is nearly fully densified. Consequently, grain size governs cemented carbide mechanical properties. WC coarsening diminishes grain

boundary density while promoting crack nucleation [26], which therefore leads to the decrease in K_{IC}.

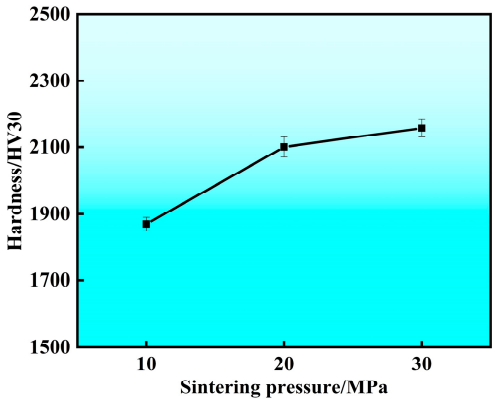

Figure 9. The hardness of WC–Co cemented carbides sintered under different pressures.

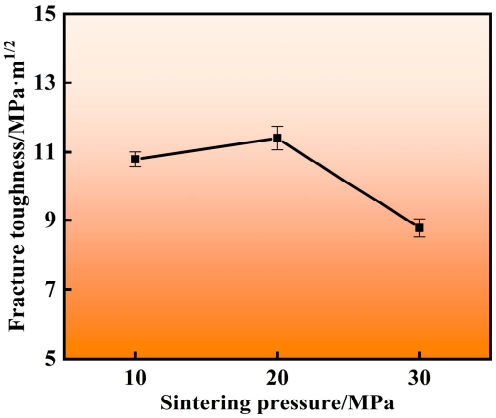

Figure 10. Fracture toughness (K_{IC}) of WC–Co cemented carbides under varied sintering pressures.

Figure 11 illustrates the crack propagation of cemented carbides after hardness testing. The results show that when sintered with a pressure of 10 MPa, cracks propagate along grain boundaries, indicating the intergranular fracture mode. Meanwhile, the propagation of the cracks requires less energy, which lowers the fracture toughness of the cemented carbides [27]. When the pressure increases to 20 MPa, the increased densification of the cemented carbides and the refinement of WC grains increase the grain boundary area. Under these conditions, enhanced crack deflection and energy dissipation during propagation improve cemented carbide toughness [28,29]. However, at 30 MPa sintering pressure, diminished crack deflection reduces fracture toughness. This phenomenon is closely associated with variations in grain size and grain boundary strength. Grain coarsening leads to a reduced number of grain boundaries, consequently weakening grain boundary binding capacity and facilitating crack initiation and propagation along grain boundaries. Additionally, the angular morphology of coarsened WC grains contributed to local stress concentration, which serves as crack initiation sites [30] within the cemented carbides. Concurrently, elevated pressure promotes intragranular defects (such as dislocation pile-ups), degrading cemented carbide fracture toughness.

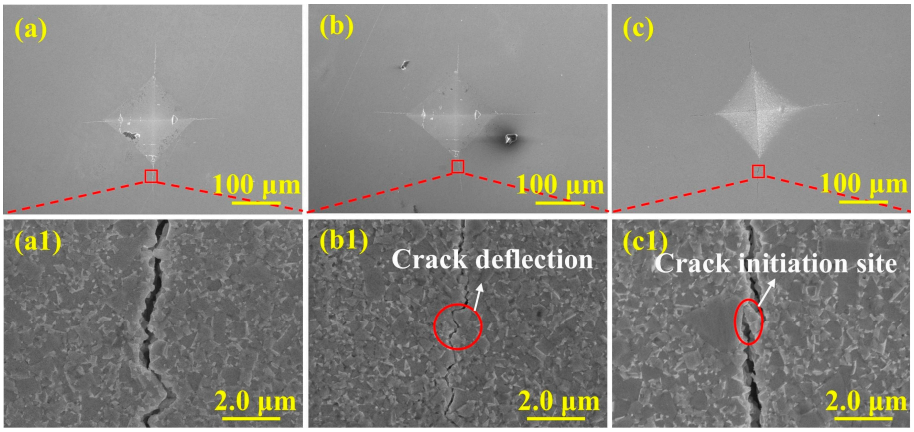

Figure 11. Vickers indentation morphology and crack propagation in WC–Co cemented carbides at different sintering pressures: (**a**,**a1**) 10 MPa, (**b**,**b1**) 20 MPa, and (**c**,**c1**) 30 MPa.

3.4. Effects of Cobalt Content Variation on the Mechanical Properties of WC–Co Cemented Carbides

Microstructural evolution and grain size distributions of SPS-sintered WC–Co cemented carbides (Co: 3/5/8 wt.%; 20 MPa, 1430 °C, 5 min) are shown in Figure 12. WC–3 wt.% Co specimens exhibit inadequate Co-phase distribution, failing to isolate WC grains. The resulting high contiguity enables WC grain coalescence and subsequent coarsening [31], which can be seen in Figure 12(a2). When the Co content is increased to 5 wt.%, most intergranular spaces are filled by the Co phase, reducing WC grain coalescence. Concomitantly, WC grain size undergoes refinement. When Co content increases to 8 wt.%, a sufficient liquid phase promotes the dissolution of small grains and effectively inhibits WC grain coalescence, leading to a uniform grain size distribution. These results demonstrate that with increasing Co content, the filling of Co between WC grains becomes more sufficient and the isolation effect becomes more pronounced, which decreases WC grain contiguity and improves grain boundary distinctness [32].

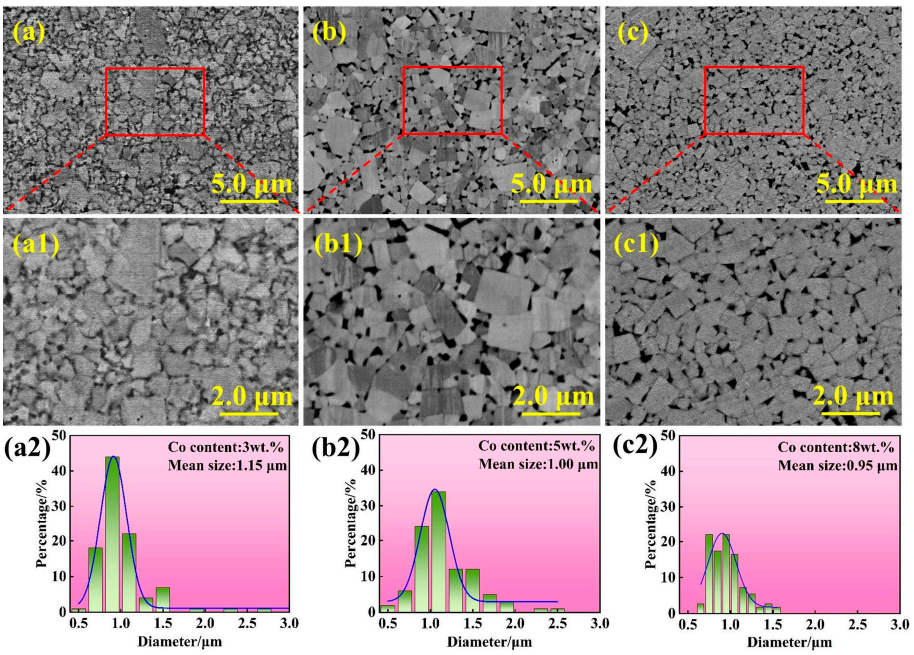

Figure 12. Microstructure and grain distribution of WC cemented carbides with different Co contents: (**a**,**a1**,**a2**) WC–3 wt.% Co; (**b**,**b1**,**b2**) WC–5 wt.% Co; (**c**,**c1**,**c2**) WC–8 wt.% Co.

Figure 13 details Vickers hardness evolution in WC–Co cemented carbides versus cobalt content. The WC–3 wt.% Co specimen achieves peak hardness (2114.3 HV30), declining to 2050.7 HV30 at 5 wt.% Co and 1874.2 HV30 at 8 wt.% Co. This inverse correlation confirms that hardness decreases with increasing cobalt content under constant sintering conditions.

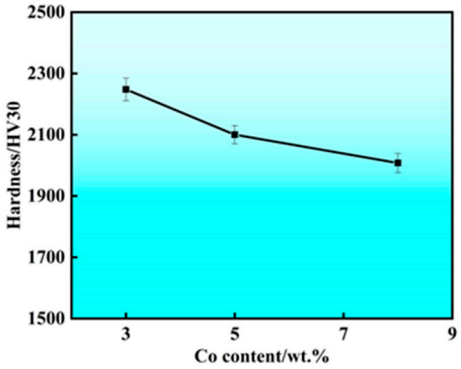

Figure 13. The hardness of WC cemented carbides with different Co contents.

Figure 14 displays fracture toughness (K_{IC}) evolution in WC cemented carbides versus cobalt content, revealing progressive enhancement with higher Co concentrations. At 3 wt.% Co, K_{IC} measures 9.57 MPa·m$^{1/2}$. At 5 wt.% Co, fracture toughness increases to 11.11 MPa·m$^{1/2}$, reaching a maximum of 13.77 MPa·m$^{1/2}$ at 8 wt.% Co. Compared to cemented carbides prepared via the powder mixing process followed by SPS sintering, the fracture toughness is increased by 2.47 MPa·m$^{1/2}$ while maintaining identical hardness [33]. This improvement is attributed to increased volume fraction and optimized distribution of the γ-phase with higher Co contents. The γ-phase exhibits superior deformation compatibility, which facilitates motion and multiplication of the dislocation during plastic deformation. This deformation accommodates internal stresses [34], thereby enhancing fracture toughness K_{IC}.

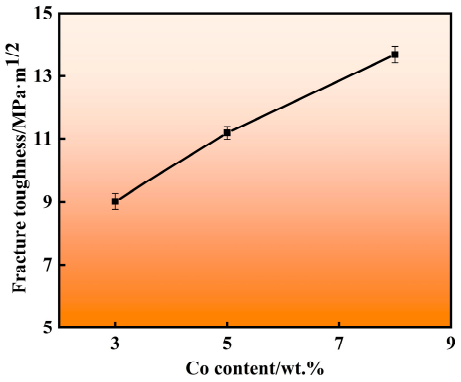

Figure 14. The fracture toughness of WC cemented carbides with different Co contents.

4. Conclusions

In this study, WC–Co cemented carbides were produced by SPS using WC–Co composite powders prepared through the electroless plating method. The effects of sintering pressure and Co content on the microstructure and mechanical properties were analyzed and the following conclusions were obtained.

(1) After non-precious metal activation pretreatment, defects such as stacking faults and dislocations were generated on the WC powder surface. This helped to decrease the nucleation energy barrier of Co during electroless plating. As a result, the Co-coated WC composite powders with core–shell structures were prepared by electroless plating.

(2) During SPS sintering, increased sintering pressure enhances the densification of WC–Co cemented carbides. At 20 MPa pressure, the flowability of liquid Co is significantly improved, which effectively reduces porosity while increasing the relative density of the cemented carbides. Simultaneously, refined WC grains improve hardness and fracture resistance through Hall–Petch strengthening.

(3) With increasing Co content, the fracture toughness of WC cemented carbides increased while the hardness decreased. Among the three compositions with distinct Co contents, the WC–8Co sample demonstrates optimal overall performance, exhibiting 1874.2 HV30 hardness coupled with 13.77 MPa·$m^{1/2}$ fracture toughness.

Author Contributions: Conceptualization, J.J., H.X. and L.Z.; methodology, J.J., H.X., D.D., Y.X. and J.S.; formal analysis, J.J., H.X., J.L., Y.X. and J.S.; investigation, J.J., H.X., D.D., Y.X. and J.S.; resources, D.H., J.L. and L.Z.; data curation, D.H., J.L. and Y.X.; writing—original draft preparation, J.J., D.D. and J.S.; writing—review and editing, H.X.; visualization, J.L.; project administration, D.H.; funding acquisition, D.H., D.D. and L.Z. All authors have read and agreed to the published version of the manuscript.

Funding: This research was funded by the Key R&D Program of Zhejiang Province, grant number 2024C01154.

Data Availability Statement: The original contributions presented in this study are included in the article. Further inquiries can be directed to the corresponding authors.

Conflicts of Interest: Author Jiangpeng Lou was employed by the company Hengdian Group DMEGC Magnetics Co., Ltd. The remaining authors declare that the research was conducted in the absence of any commercial or financial relationships that could be construed as a potential conflict of interest.

References

1. Spalden, M.V.; Pötschke, J.; Michaelis, A. Novel Route for Preparing Diamond-Enhanced Cemented Carbides via Reactive Sintering. *Metals* **2023**, *13*, 1908. [CrossRef]
2. Premjarunan, S.; Tuchinda, K.; Worasaen, K. Study on the Effects of Cryogenic Treatment on WC-Co Cemented Carbide at Different Scales Using an Indentation Technique. *Metals* **2025**, *15*, 297. [CrossRef]
3. Yu, S.B.; Min, F.; Li, D.; Noudem, G.J.; Zhang, H.L.; Ma, J.C.; Zhao, K.; Yao, Z.; Zhang, J. Comparative Study on Microstructure and Mechanical Properties of Coarse-Grained WC-Based Cemented Carbides Sintered with Ultrafine WC or (W+C) as Additives. *J. Wuhan Univ. Technol.-Mat. Sci. Edit.* **2024**, *39*, 399–409. [CrossRef]
4. Li, C.; Li, T.L.; Zhang, X.H.; He, T.Z.S.; Su, L.Z.; Wen, D.D.; Shao, S.Z.; Cai, X.; Cao, Q.Z. Investigating the Influence of Laser-Etched Straight and Wavy Textures on Grinding Efficiency and Tool Quality of WC-Co Carbide Cutting Tools. *Materials* **2025**, *18*, 528. [CrossRef]
5. Fan, Y.; Li, Z.; Hao, Z. Study on Interface Characteristics of WC-Co Doped Y Rare Earth Element Cemented Carbide Cutting Tool and Its Influence on Material Properties. *Mater. Sci. Technol.* **2025**, *41*, 962–974. [CrossRef]
6. Tang, X.; Mao, R.; Zhang, F.; Jin, Y.; Zhou, W.; Su, W.; Jiang, W.; Wang, J. Optimizing WC-10Co Cemented Carbides with High-Entropy (Ti, Cr, V, Nb, Mo)(C, N) Inhibitor: Microstructure, Mechanics, and Wear Resistance. *J. Alloy Compd.* **2025**, *1037*, 182148. [CrossRef]
7. Muraliraja, R.; Selvan, R.A.S.; Selvakumar, A.; Franco, M.; Tamilarasan, T.R.; Sanjith, U.; Sha, W.; Sudagar, J. A Review of Electroless Coatings on Non-Metals: Bath Conditions, Properties and Applications. *J. Alloy Compd.* **2023**, *960*, 170723. [CrossRef]
8. Yang, X.H.; Wang, K.F.; Chou, K.C.; Zhang, G.H. Preparation of Low Binder WC-Co-Ni Cemented Carbides with Fine WC Grains and Homogeneous Distribution of Co/Ni. *Mater. Today Commun.* **2022**, *30*, 103081. [CrossRef]
9. Buravleva, A.A.; Fedorets, A.N.; Vornovskikh, A.A.; Ognev, A.V.; Nepomnyushchaya, V.A.; Sakhnevich, V.N.; Lembikov, A.O.; Kornakova, Z.E.; Kapustina, O.V.; Tarabanova, A.E.; et al. Spark Plasma Sintering of WC-Based 10wt.%Co Hard Alloy: A Study of Sintering Kinetics and Solid-Phase Processes. *Materials* **2022**, *15*, 1091. [CrossRef]
10. Wang, Y.; Xiang, F.M.; Yuan, X.B.; Yang, B.B.; Wang, F.L.; Li, Y.P. Effects of Processing Parameters on the Microstructure and Mechanical Properties of Nanoscaled WC-10Co Cemented Carbide. *Materials* **2022**, *15*, 4472. [CrossRef]
11. Sun, X.G.; Wang, Y.; Li, D.Y. Mechanical Properties and Erosion Resistance of Ceria Nano-Particle-Doped Ultrafine WC–12Co Composite Prepared by Spark Plasma Sintering. *Wear* **2013**, *301*, 406–414. [CrossRef]

12. Yang, Q.M.; Yang, J.A.; Wen, Y.; Zhang, Q.Y.; Chen, L.Y.; Chen, H. A Novel Route for the Synthesis of Ultrafine WC-15 wt. %Co Cemented Carbides. *J. Alloy Compd.* **2018**, *748*, 577–582. [CrossRef]
13. Su, W.; Luo, W.; Lu, J.H.; Zeng, S.J.; Zhou, W.X. Coarse-Grained WC–6Co Hardmetals with Dual-Scale and Plate-like WC Structures Fabricated by Convention Powder Metallurgy Process. *Int. J. Refract. Met. Hard Mater.* **2024**, *125*, 106886. [CrossRef]
14. Zhu, L.; Wang, J.F.; Tu, Z.B.; Xue, N.; Li, W.W. Effects of Powder Microscopic Defects on Densification and Mechanical Properties of WC via Spark Plasma Sintering. *Mater. Sci. Forum.* **2021**, *5994*, 1770–1777. [CrossRef]
15. Wang, J.F.; Zuo, D.W.; Zhu, L.; Tu, Z.B.; Dai, S. Preparation of low Co-coated WC composite powder by electroless plating and its sintering by spark plasma sintering process. *T. Mater. Heat Treat.* **2016**, *37*, 12–17. [CrossRef]
16. Guo, L.; Xiao, L.R.; Zhao, X.J.; Song, Y.F.; Cai, Z.Y.; Wang, H.J.; Liu, C.B. Preparation of WC/Co Composite Powders by Electroless Plating. *Ceram. Int.* **2017**, *43*, 4076–4082. [CrossRef]
17. Tong, J.; Zhang, J.F.; Wang, Y.; Min, F.L.; Wang, X.Y.; Zhang, H.L.; Ma, J.C. Preparation of Co-Plated WC Powders by a Non-Precious-Co-Activation Triggered Electroless Plating Strategy. *Adv. Powder Technol.* **2019**, *30*, 2311–2319. [CrossRef]
18. He, R.G.; Li, B.; Ou, P.H.; Yang, C.H.; Yang, H.L.; Ruan, J.M. Effects of Ultrafine WC on the Densification Behavior and Microstructural Evolution of Coarse-Grained WC-5Co Cemented Carbides. *Ceram. Int.* **2020**, *46*, 12852–12860. [CrossRef]
19. Voorhees, P.W. The Theory of Ostwald Ripening. *J. Stat. Phys.* **1985**, *38*, 231–252. [CrossRef]
20. Wu, Z.C.; Ye, N.; Zhuo, H.O.; Mao, J.; Zhu, W.T.; Gong, Z.Y.; Chen, X.L.; Tang, J.C. High-Pressure and High-Temperature Synthesis of Binder less Nanocrystalline WC Cemented Carbide: Microstructure and Mechanical Properties. *Ceram. Int.* **2025**, *51*, 7756–7765. [CrossRef]
21. Fan, X.Q.; He, D.W.; Wang, P.; Li, D.; Liu, Y.J.; Ma, D.J.; Du, Y.C.; Gao, S.P.; Kou, Z.L. High Pressure Infiltration Sintering Behavior of WC-Co Alloys. *High Press. Res.* **2016**, *36*, 585–594. [CrossRef]
22. Bonache, V.; Salvador, M.D.; Fernández, A.; Borrell, A. Fabrication of Full Density Near-Nanostructured Cemented Carbides by Combination of VC/Cr3C2 Addition and Consolidation by SPS and HIP Technologies. *Int. J. Refract. Met. Hard Mater.* **2011**, *29*, 202–208. [CrossRef]
23. Lu, Z.C.; Wang, W.; Zeng, M.Q.; Zhu, M. Breaking the Hardness-Toughness Trade-off in WC-Co Hard metals: Introduction of Dual-Scale Plate-like WC and Modification of Prediction Models. *Int. J. Refract. Met. Hard Mater.* **2022**, *108*, 105910. [CrossRef]
24. Cha, S.I.; Hong, S.H.; Kim, B.K. Spark Plasma Sintering Behavior of Nanocrystalline WC-10Co Cemented Carbide Powders. *Mater. Sci. Eng. A* **2003**, *351*, 31–38. [CrossRef]
25. Siwak, P.; Garbiec, D. WC-5Co Cemented Carbides Fabricated by SPS. *Arch. Metall. Mater.* **2018**, *63*, 2031–2037. [CrossRef]
26. Müller, D.; Konyashin, I.; Farag, S.; Ries, B.; Zaitsev, A.A.; Loginov, P.A. WC Coarsening in Cemented Carbides during Sintering. Part I: The Influence of WC Grain Size and Grain Size Distribution. *Int. J. Refract. Met. Hard Mater.* **2022**, *102*, 105714. [CrossRef]
27. Yadav, S.; Zhang, Q.F.; Behera, A.; Haridas, R.S.; Agrawal, P.; Gong, J.D.; Mishra, R.S. Role of Binder Phase on the Microstructure and Mechanical Properties of a Mechanically Alloyed and Spark Plasma Sintered WC-FCC HEA Composites. *J. Alloy Compd.* **2021**, *877*, 160265. [CrossRef]
28. Chen, W.Y.; Yin, Z.B.; Li, X.L.; Yuan, J.T. Effect of Co-Doped Additives on Microstructure and Mechanical Properties of Microwave-Sintered WC-10Co Cemented Carbide Tool Materials. *J. Alloy Compd.* **2023**, *962*, 171148. [CrossRef]
29. Ye, Y.; Xia, H.; Lin, Y.; Chen, F.; Shen, Q. Refined WC Grain Size and Improved Mechanical Properties in a Hardmetal WC-8Co Processed via Short-Time Semi-Solid Hot Pressing. *J. Alloy Compd.* **2021**, *889*, 161560. [CrossRef]
30. Chermant, J.L.; Osterstock, F. Fracture Toughness and Fracture of WC-Co Composites. *J. Mater. Sci.* **1976**, *11*, 1939–1951. [CrossRef]
31. Garcia, J.; Cipres, V.C.; Blomqvist, A.; Kaplan, B. Cemented Carbide Microstructures: A Review. *Int. J. Refract. Met. Hard Mater.* **2019**, *80*, 40–68. [CrossRef]
32. Saito, H.; Iwabuchi, A.; Shimizu, T. Effects of Co Content and WC Grain Size on Wear of WC Cemented Carbide. *Wear* **2006**, *261*, 126–132. [CrossRef]
33. Tian, X.; Liang, Y.; He, G.; Zeng, L. Reduced Graphene Oxide and Alumina Synergistically Enhance the Mechanical and Wear Properties of WC-8Co Cemented Carbide. *Int. J. Refract. Met. Hard Mater.* **2023**, *113*, 106184. [CrossRef]
34. Yin, C.; Ruan, J.M.; Du, Y.; Long, J.Z.; Peng, Y.B.; Li, K. Effects of Cr3C2, VC, and TaC on Microstructure, WC Morphology and Mechanical Properties of Ultrafine WC-10 Wt.% Co Cemented Carbides. *Metals* **2020**, *10*, 1211. [CrossRef]

Disclaimer/Publisher's Note: The statements, opinions and data contained in all publications are solely those of the individual author(s) and contributor(s) and not of MDPI and/or the editor(s). MDPI and/or the editor(s) disclaim responsibility for any injury to people or property resulting from any ideas, methods, instructions or products referred to in the content.